J. Eur. Opt. Society-Rapid Publ. 2026, **22**, 51

https://doi.org/10.1051/jeos/2026047
Available online at: https://jeos.edpsciences.org

Journal of the European Optical Society-Rapid Publications

RESEARCH ARTICLE OPEN ACCESS

Modeling and experimental comparison of the plasma jet induced etch front for subsurface damage determination

Heike Müller[1,*], and Thomas Arnold[1,2]

[1] Leibniz Institute of Surface Engineering (IOM), Permoserstraße 15, 04318 Leipzig, Germany
[2] Institute of Manufacturing, TU Dresden, 01062 Dresden, Germany

Received 25 March 2026 / Accepted 15 May 2026

Abstract. The performance of optical systems can be compromised by subsurface damage (SSD) caused by mechanical processing. This study presents a destructive method of determining SSD depth in fused silica surfaces using atmospheric plasma jet etching (PJE). A simplified mathematical model describes how the etching front evolves under the assumption of isotropic etching. By comparing simulated surfaces with topographies determined experimentally after each etching step, an isotropy factor (IF) is calculated to identify deviations from isotropy. Areas with an IF greater than one exhibit anisotropic etching behavior, indicating the presence of SSD. The method was validated using defined Vickers indentations, scratches and conventionally polished samples. The maximum SSD depth correlates with both the maximum IF value and the slope of the cavity volume versus etching depth. For the samples examined, SSD depths ranged from 6.37 µm to 52.47 µm. The results agreed well with OCT measurements (deviation < 10%). The developed approach not only enables the quantitative determination of SSD depth, but also the three-dimensional reconstruction of crack morphology. Combining computer-aided modelling with experimental comparison provides a robust method for characterizing the quality of optical components.

Keywords: Atmospheric plasma jet, Plasma jet etching, Subsurface damage, Fused silica.

1 Introduction

The performance of optical systems is continuously improving as a result of a combination of different optical elements, advances in component design and materials, and higher precision of manufacturing techniques. However, numerous factors such as misalignment, coating defects and subsurface damage (SSD) can affect this theoretically high quality. Subsurface damage describes microcracks that occur, for example, as a result of the abrasive surface machining of hard, brittle optical materials (e.g. glass). During the grinding process of optical glass, the abrasive grains cause the material to chip. These random fractures initially result in an optically opaque surface, which later becomes transparent during the subsequent polishing process. However, the grinding process also causes median cracks that extend into the matrix below the chipping and must also be removed by polishing [1]. It is therefore important to know the maximum depth of the defects.

In optics manufacturing, the SSD depth is estimated by the optical engineer during the manufacturing process based on the machining parameters used and the roughness after grinding in order to determine the required material removal during polishing. With sufficient experience, the required polishing removal can be estimated to ensure that the optical element at the end no longer exhibits SSD. Other non-destructive methods are based on light scattering effects caused by damage buried under the defect-free surface. Laser scattering methods such as laser scanning confocal microscopy or total internal reflection microscopy are used as well as optical coherence tomography (OCT) or X-ray diffraction. For the latter, the equipment is very expensive and requires a vacuum pumping system which impedes sample handling, so this technique is rarely used for SSD determination [2–4].

In addition to the development of non-destructive testing methods, destructive testing is still state of the art. Most of these techniques are based on the preparation of a cross-sectional view, such as bevel or dimple polishing but also focused ion beam (FIB) to determine the depth-extent of the damage by microscopic observation (e.g. optical microscopy or transmission electron microscopy). Those preparation techniques can only give information about a specific cross-sectional view. A more global distribution of the SSD can be detected after applying wet chemical etching

* Corresponding author. heike.mueller@iom-leipzig.de

methods. Despite the knowledge of its health risks, hydrofluoric acid (HF) is still applied for experiments [5–7]. However, meanwhile potassium hydroxide (KOH) solution replaces the highly toxic HF, even though KOH is still very corrosive [3, 8, 9]. The etching process leads to a crack expansion which requires precise control to accurately correlate removal and damage depth [10].

A number of researchers have been investigated the surface effects that are affected by chemical etching. The focus is currently still on wet chemical etching, where efforts are being made to understand the etching effect and create models based on specific processes, e.g., hydrofluoric-based etching. This resulted in several publications over the last years on the topic of modelling mainly the isotropy of etching processes. Such models are based on finite elements approaches. In 1990, Katardjiev et al. used numerical analysis to investigate the development of semiconductors surface during the growth and removal [11]. They applied the Huygens principle of wavefront propagation, which states that every point on a wavefront is the starting point of a new wave. These elementary waves overlap to form a new wavefront. Almost 30 years later, this approach was applied to describe the expanding of scratches during wet chemical etching of fused silica with a finite element model [12]. Lui et al. investigated the hydrofluoric acid-based etching effect on surface defects of FS optics [6]. They performed finite difference time domain (FDTD) simulations and proposed a local-curvature-dependent model to explain etching rates on rough surfaces [6]. In a comparison of wet chemical etching and dry etching by medium pressure plasma process, Krishna et al. concluded that overall both processes are isotropic, while the kind of attacks differ [13]. With the applied dry etching process in medium-pressure setting, the first removal can be seen at the peaks which as a result decrease, while chemical wet etching causes a uniform enlargement of the holes, laterally and in depth [13]. The influence of an atmospheric pressure plasma jet to FS having selective indentation defects, created using a Vickers test indenter was investigated by Jiao et al. [14]. Based on the simulation results of the 3D-level-set method, the research group was able to confirm the isotropic etching process of FS, which, however, also exhibits anisotropic properties at the crack edges [14]. These studies focus mainly on defect models or measured individual defects and their progress at shallow etching depths.

As an alternative, the application of the atmospheric plasma jet (PJ) provides a controlled, local etching process with almost less health risks. PJ technology has been established for more than two decades, mainly applied for form generation and figure error correction of freeform optics [15–18]. In this paper, we present a study on the SSD preparation in fused silica surfaces employing plasma jet etching. A simplified mathematical approach has been developed to model the isotropic etch front evolution. SSD morphology has been investigated on indentation-induced cracks, single scratch-generated defects and SSD caused by mechanical grinding. A comparison with experimental etch front determination is made, resulting in the evaluation of the lateral distribution of an isotropic etch factor. With the help of this factor the distribution of SSD depths can be determined.

2 Experimental

Targeted material removal was obtained by dry chemical etching applying an atmospheric pressure PJ. Since the process details have already been described in numerous publications [16, 17, 19], only a few main facts will be given. The PJ source is based on a coaxial conductor system where the main process gases helium (He), oxygen (O_2), and tetrafluoromethane (CF_4) are supplied through the inner conductor. Nitrogen (N_2), affecting as shield gas, is supplied peripherally. The plasma discharge is ignited at the nozzle by excitation with microwave energy (MW, $f \approx$ 2.48 GHz). The generated PJ interacts with the sample surface converting SiO_2 into gaseous products SiF_4 and O_2 which causes the material removal. The PJ source operates in a conventional CNC motion system. Etching is performed stepwise where the etching depth varies for the different types of defects. Using this method, it is possible to successively expose cracks reaching into the material. Smaller etching depth increments provide more detailed information about the etching mechanism, while larger increments enable deeper etching to be achieved more quickly.

3 Material and methods

Etching experiments have been performed on fused silica samples of size 40 × 40 × 10 mm (Corning Inc.). In order to generate defined SSD characteristics, two different methods were used. Static indentations by a Vickers tip, schematically shown in Figure 1A and a scratch test device applying a Rockwell-Diamond tip given in Figure 1B were employed to imitate an abrasive grain moving over the sample surface. Mechanical preparation of the samples was done by University of Applied Sciences in Jena.

In order to prove the developed method for SSD depth determination, it was finally applied to a mechanically ground and polished sample (diameter: 50 mm / thickness: 8.3 mm) provided by Layertec GmbH.

3.1 Surface topography measurements

After each plasma jet etching step, the surface topography was measured using white light interferometer (WLI, NPflex, Bruker Corp.). For cases where WLI was not applicable due to strong surface gradients leading to data dropout, a confocal microscope (µsurf explore, NanoFocus AG) was employed. The confocal microscope provided more information about the shape, especially of deep indentations with steep sidewalls. The field of view was 231 × 173 μm^2 for WLI measurements and 320 × 320 μm^2 for the confocal microscope, respectively. In preliminary tests the correspondence of the results obtained from both measurement devices was proven.

3.2 Etch front calculation method

To model the local removal during plasma treatment assuming isotropic etching, the etch front was simulated starting at a measured surface topography described by

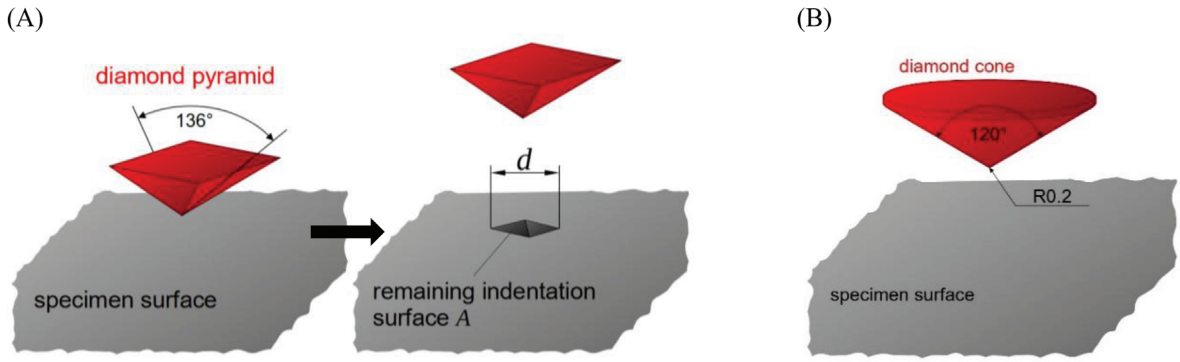

Figure 1. Schemes of applied geometries for defined inducing of SSD in fused silica samples: (A) Vickers indentation [20] and (B) Rockwell-Diamond [21] for scratches.

the coordinates $P_0 = [x_0, y_0, z_0]$. By calculating the surface normal for each point $N_0 = [n_{x,0}, n_{y,0}, n_{z,0}]$ the evolving surface at a time step Δt is obtained by:

$$P_i = P_0 + N_{i-1}\, r\Delta t \qquad i = 1 \ldots k \tag{1}$$

where r is the etching rate in µm/s and Δt is an appropriately chosen small time step. Hence, the total etching depth at positions with surface normal $[0, 0, -1]$ is $d = i \cdot r \cdot \Delta t$. After each iteration step i the obtained surface coordinates P_i are interpolated to the grid (x_0, y_0) yielding a local etch depth z_i, followed by a Gaussian filter of width to slightly smooth the surface. Although the smoothing filter has no strict physical meaning, such smoothing acts as a simplified approach to a microscopic isotropic etching effect mimicking the Huygens-principle of elementary wavelets as described in [12].

The calculation scheme has been implemented in a self-written Matlab® script (The MathWorks, Inc.). As an example, the projection of normals of a 2D V-groove is shown in Figure 2A. By adjusting the iteration number i at a given etching rate r and time step Δt a prospective isotropic removal and topography, respectively, can be simulated. Figure 2B shows the development of the V-groove with progressive etching. In order to be able to map both, small and large removal depths, with a comparable accuracy, the calculation was performed in several defined steps of about 1 µm.

After the calculation of an isotropically etched surface $z^{\mathrm{calc}}(x, y)$ based on the initial topography z_0, the result is compared by the experimentally obtained surface z^{exp} after etching to the same depth. As the areal measurements of two consecutive PJE steps do not perfectly overlap due to slight lateral mismatch in the microscope, the lateral alignment was corrected by a Matlab® image recognition routine prior to performing the calculation. All pixels of z^{exp} that do not match the original z_0 were set to zero and can therefore influence the subsequent calculation. Since this effect only occurs in the peripheral area, which is approximately zero for the leveled surface measurement, its influence on the subsequent calculation can be neglected. The flowchart in Figure 3 shows the procedure of data processing.

The comparison of z^{calc} and z^{exp} is done by taking the ratio given in equation (2) where IF can be designated as isotropic factor.

$$IF(x, y) = \frac{z^{exp}(x, y)}{z^{calc}(x, y)} \tag{2}$$

Thus, the experimental result of a PJE step is related to the calculated result, assuming isotropic etching with the same etching removal d. A value $IF \approx 1.0$ indicates loci of isotropic etching in the experiment, while values $IF > 1$ indicate loci of anisotropic etching. The greater the deviation from 1, the stronger the anisotropic removal. Provided that morphological distortions in the surface are anisotropically etched by the plasma jet, IF maps provide information on the position and the extent of SSD. To evaluate the anisotropic removal as a function of etch depth, the value IF_{mean} - calculated as the average across the entire topography – and its standard deviation are used.

In the following section the application of the procedure to different surfaces is shown.

In order to gain a more detailed understanding of the characteristics of the SSD (laterally and depth-dependent), the SSD-affected areas can be represented as 3D-plots, where the measured topography data added by the removal depth ($z^{\mathrm{exp}} + d$) are plotted for loci where IF exceeds a value of 1, i.e. for anisotropically etched regions.

4 Results

4.1 Vickers imprints

Localized indentations generated by a Vickers indenter exhibit a widespread damage shape, with the lateral expansion being approximately twice as large as the measurable depth, as shown exemplarily for the initial measurement of indentation of Sample #1 in Figure 4.

Since the increasing etching depth leads to further expansion of the indentation [14], the void volume VV was analyzed after each process step. Equation (3) specifies the mathematical description where Z is the height value after removing the tilt of the areal measurement with respect to the area that is not affected by the indentation.

$$VV = \sum_{Z \leq 0} Z(X, Y) \cdot dXdY \tag{3}$$

To quantify the SSD depth the roughness parameter Sv, defined as maximum pit height of a topographic

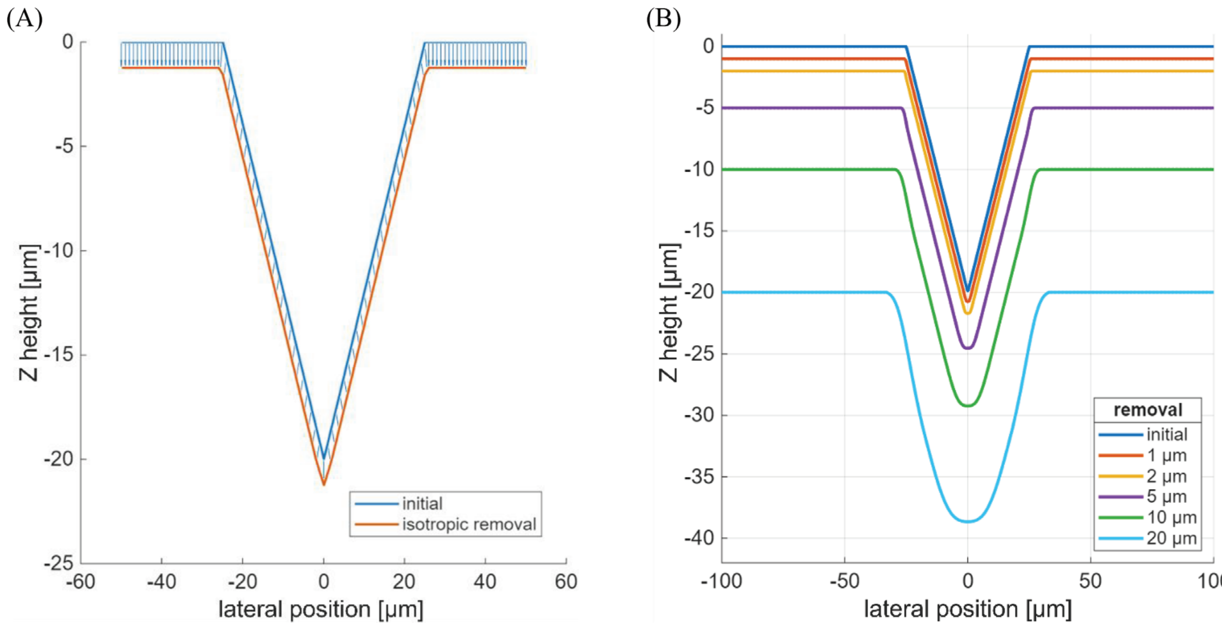

Figure 2. Approach of calculating theoretical surface topographies with progressive etching given for simplified 2D-plots: (A) Surface normal direction (blue arrows) as a function of the initial profile resulting in the new profile after isotropic removal and (B) development of a V-shaped groove for increasing removal depths.

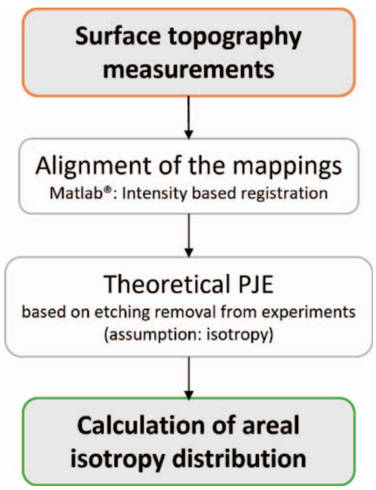

Figure 3. Flow chart.

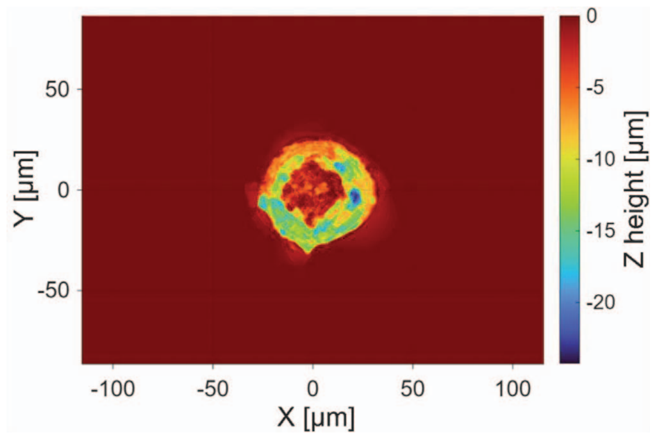

Figure 4. Initial topography measurement of indentation of Sample #1showing its lateral extent and depth.

measurement, is determined. Previous studies have shown that the maximum SSD occurs where the first derivative of this determining variable, plotted over the etching depth, shows a sign change [22]. Consequently, after each etching step, the slope S_{VV} is calculated using equation (4), where VV is the void volume and d the etching depth.

$$S_{VV} = \frac{VV_{PJE_n} - VV_{PJE_{n-1}}}{d_{PJE_n} - d_{PJE_{n-1}}} \tag{4}$$

The SSD depth is given where the slope S_{VV} of the void volume is at its maximum. The determination of the SSD depth given in equation (5) is finally based on maximum Sv and etching depth d.

$$SSD\,[\mu\mathrm{m}] = Sv(\max(S_{VV})) + d\,(\max(S_{VV})) \tag{5}$$

We postulate that isotropic etching occurs when there is no longer any SSD, or conversely as long as anisotropic etching is present, SSD still exists. The disturbed bulk behaves like an impure material that undergoes anisotropic etching using PJE. Figures 5A–5D exemplarily show the case of a fully isotropic removal, where the measurement is nearly identical to the calculated topography (see Figs. 5B and 5C). In the case of anisotropic removal shown as a representative example in Figures 5E–5H, a discrepancy between experimental results and the calculated topography is

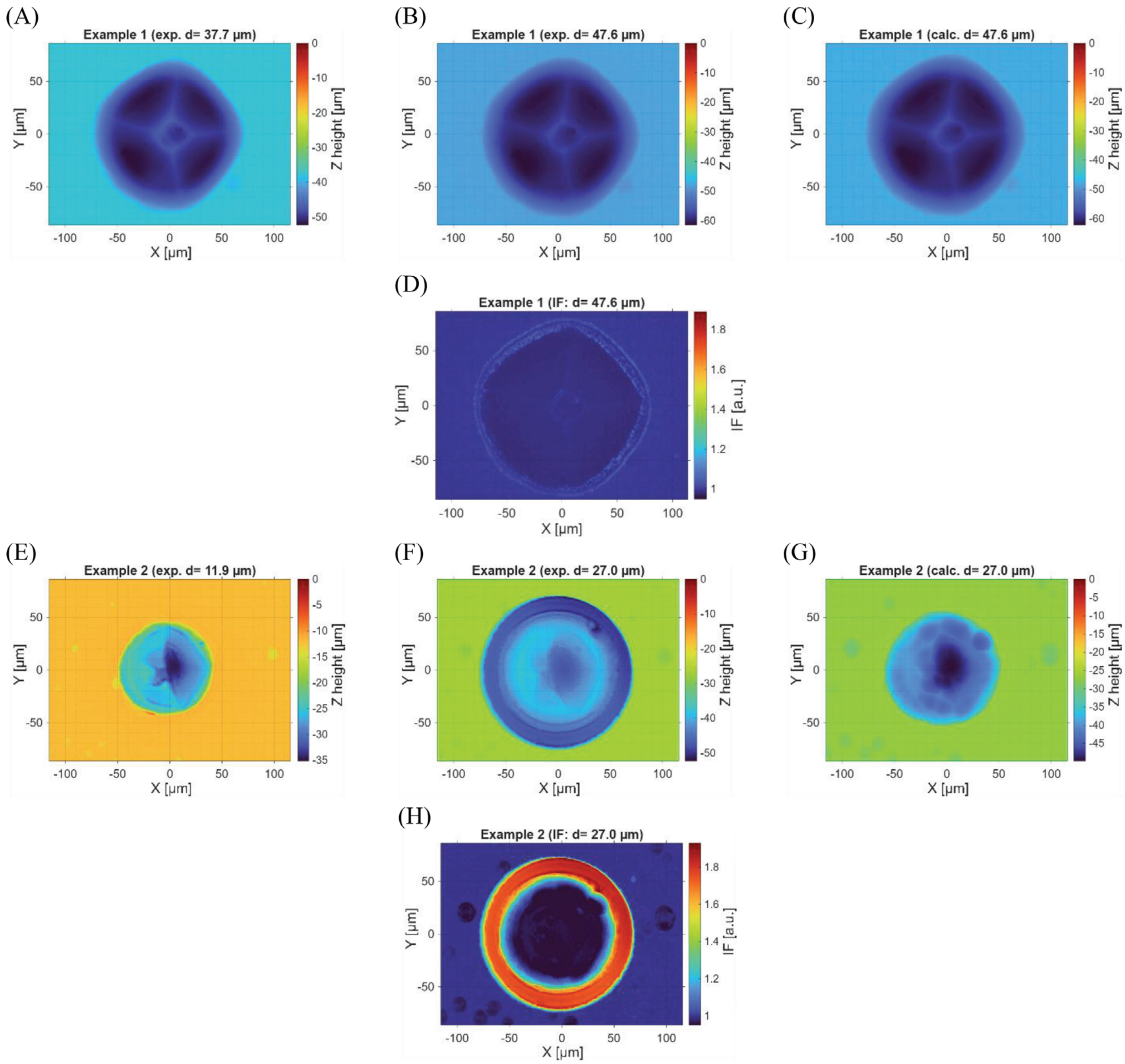

Figure 5. Comparison of measurement (A, B, E, F) to calculated isotropic etched surfaces (C, G) and the resulting map visualizing the isotropic factor *IF* (D, H). The example A–D shows nearly isotopically etched result, whereas E–H depict significant discrepancy from isotropy.

evident. Comparing the areal representations of the *IF* in Figures 5D and 5H the *IF* of the isotropic example in Figure 5D is almost 1, only a slight variation is apparent. Hence, it can be concluded that no SSD was present anymore on this sample. However, a different situation is observed in Figure 5H. In the center and at the periphery of the areal map isotropic etching prevails ($IF \approx 1$, dark blue color) while the red-colored ring clearly indicates an increased value of $IF \approx 1.8\ldots1.9$.

The isotropic factor *IF* was calculated for Sample #1. The mean value together with its standard deviation is shown in Figure 6 as a function of the etching depth. The presence of error bars indicates locally varying *IF*, since the region surrounding the indentation exhibits values of $IF \approx 1$, and the distorted areas yield higher values. The large deviation at an etching depth of 1.5 µm is due to preferential etch attack of the elevated area in the center of the initial indentation (see Fig. 4), which consists of distorted material at the surface with cracks and local stress. The slope S_{VV} is included for comparison. The error bars for the S_{VV} values result from the propagation of uncertainty based on the estimation of measurement uncertainties for the parameters d and VV, which are used to calculate the slope according to equation (4). It is obvious that the maximum of both parameters – IF_{mean} and S_{VV} – occur at the same etching depth. That indicates that the process step where the comparatively largest increase in VV occurs also corresponds to the highest level of anisotropic etching. This is obvious, since the increase of VV is caused by the deviation from isotropic etching. Therefore, the etching depth where the IF_{max} is recognized is used to calculate the SSD depth applying equation (5), yielding a value of SSD = 35.3 µm.

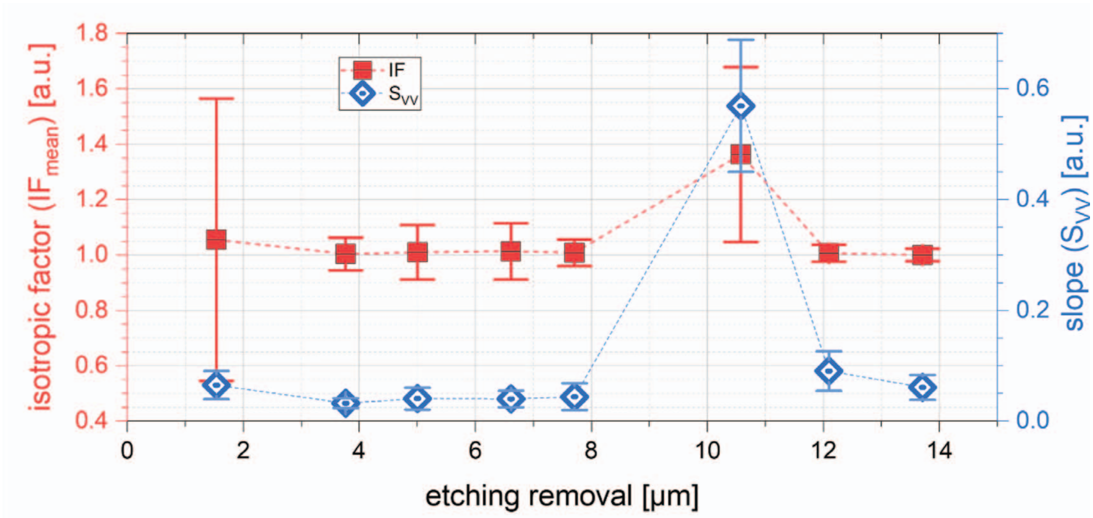

Figure 6. Comparison of calculated IF_{mean} and the slope S_{VV}, which is used to obtain the SSD depth after PJE given for Sample #1.

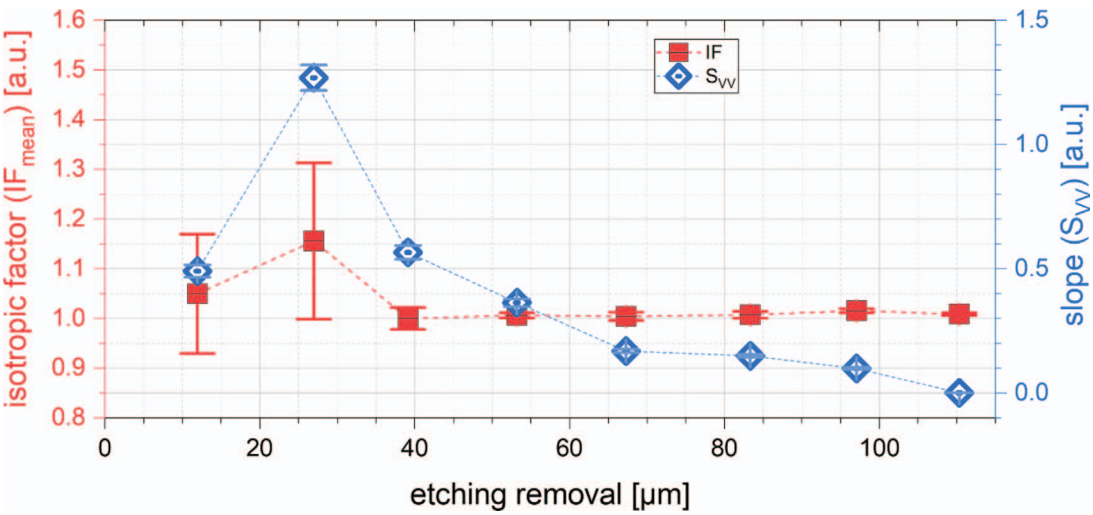

Figure 7. Comparison of calculated IF_{mean} and the slope S_{VV}, which is used to experimentally obtain the SSD depth after PJE given for Sample #2. In contrast to the previous example, here the etching steps are significantly larger.

The calculation principle is shown below for another Vickers indentation of Sample #2 (see Fig. 7). In this case, higher etching removal is achieved for each process step, so that the maximum of the slope and *IF* can already be seen in the second etching step. Nevertheless, the $IF_{\max}$ corresponds to the maximum slope at an etching depth $d \approx 27$ µm, and according to equation (6), a value SSD = 52.47 µm is determined.

In addition, *IF* can be used to generate a 3D representation of the SSD structure. As explained in Section 3.2, the measured surface topography data $z^{\exp}$ for $IF >$ threshold are combined in a height map, taking into account the corresponding removal depths *d*. Figures 8A and 8B show the results for the indentations of Sample #1 and Sample #2 for $IF > 1.5$. Both indentations exhibit a prominent ring structure located in a depth of approx. 10–15 µm. These features indicate the presence of a cone crack which mainly contributes to SSD in the samples investigated. Here, the material is distorted resulting in sudden lateral expansion. This abrupt widening might be due to a combination of chemical etching attack and gas flow. Such cone cracks could be verified by OCT measurements and are particularly noticeable for Sample #1 as shown in Figure 8C. OCT measurements given in Figures 8C and 8D were provided for comparison by the University of Applied Sciences in Jena.

The *IF* threshold used to determine surface height data is moderately sensitive. However, a useful range is to be identified that should be used to obtain valid results. To substantiate this in more detail, the height of distinctive SSD features for Sample #2 are compared in Figure 9 for different *IF* values. It is evident that for $IF > 1.1$ and $IF > 1.25$ shown in Figures 9A and 9B artifacts from the measurement and a lack of alignment accuracy occur at a z height of approx. −27 µm. Otherwise, if the threshold is set too high (Fig. 9D for $IF > 1.8$), information about the

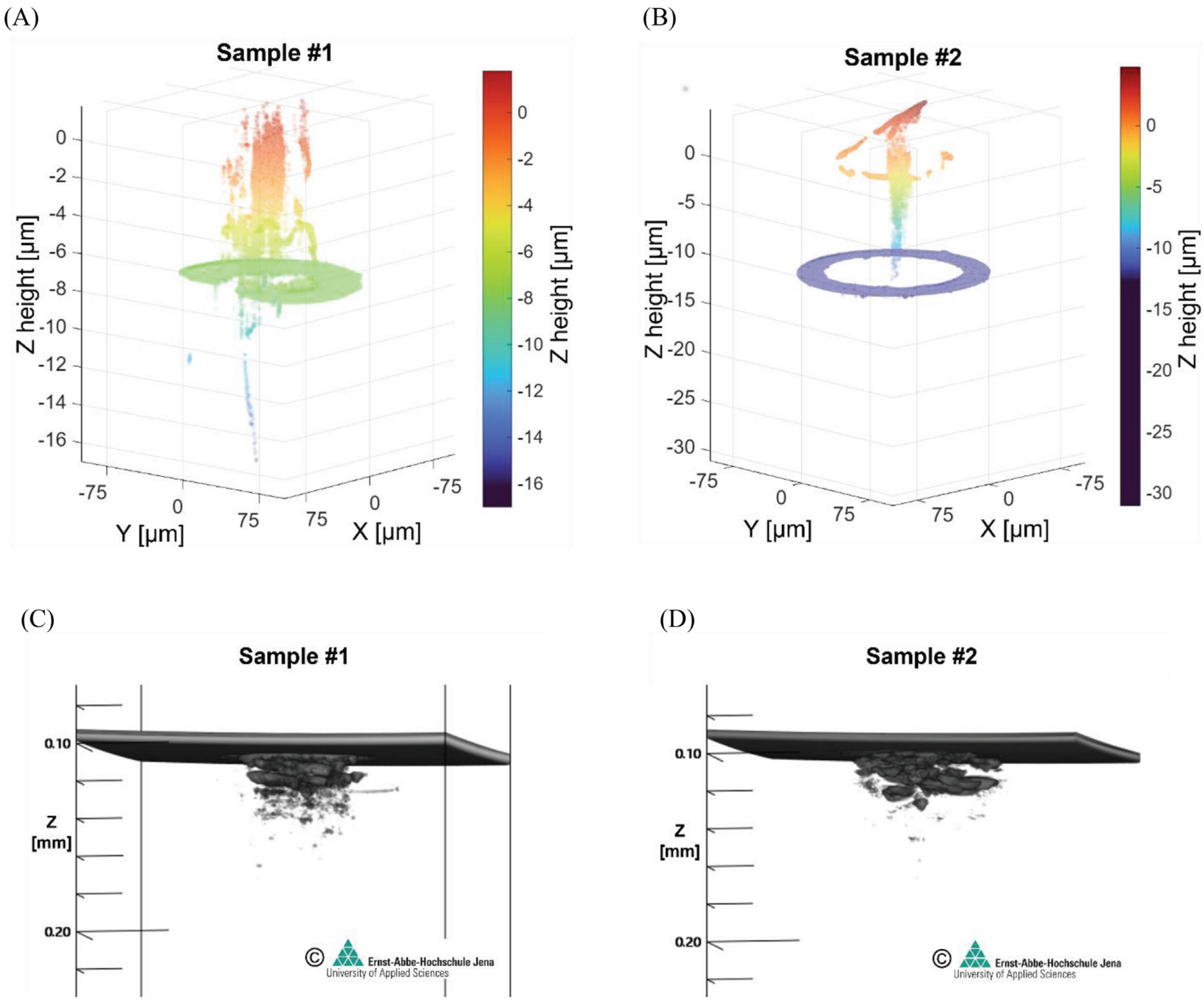

Figure 8. Three-dimensional plots for the indentations (A) Sample #1 and (B) Sample #2. The plotted surface height values are given for every pixel where $IF > 1.5$. In addition, the OCT measurements of the initial indentations (C, D) are shown for comparison.

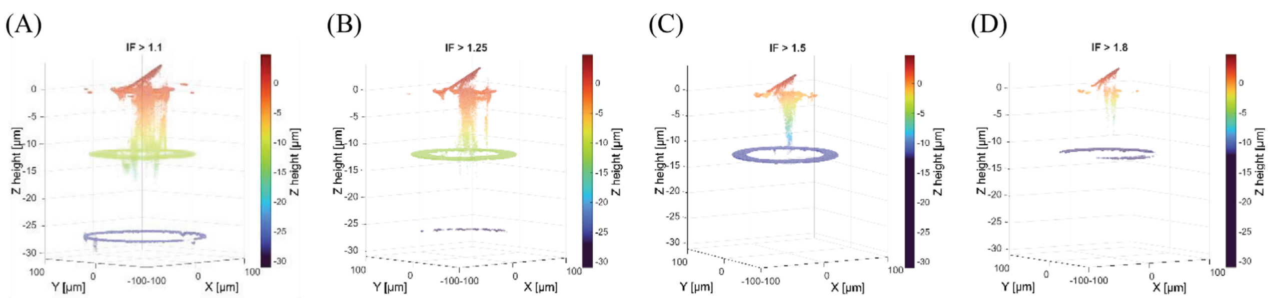

Figure 9. Visualization of the SSD-affected topography depending on the chosen IF threshold.

total extent of the prominent ring at z height of −11.8 µm is missing, which clearly occurs in Figure 9C for an IF threshold set to 1.5.

Finally, the impact of the IF threshold on the determination of the SSD depth is shown. Figure 10A reveals that the choice of the IF values has only a marginal influence on the resulting SSD depth. For small etching steps, as given for Sample #1 (see Fig. 6), the determined SSD depth changes for $IF > 3.0$ for the first time. For larger etching removal in the case of Sample #2 shown in Figure 7, the influence is slightly higher. Here, the change of the SSD depth appears already for $IF > 1.9$. Overall, the SSD depth calculated with $IF > 1.5$, which was also applied before to visualize the SSD-affected topography, matches the results

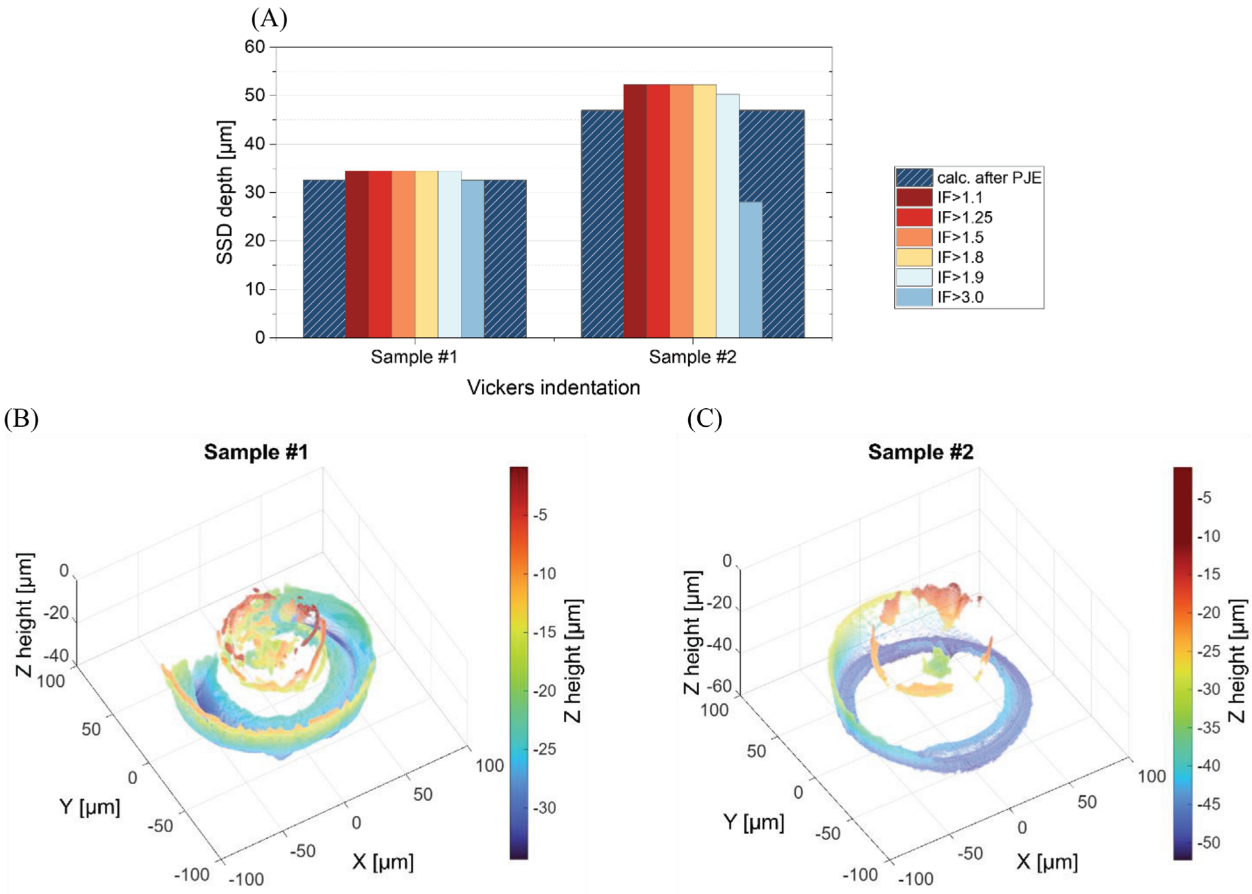

Figure 10. Determination of the SSD depth: (A) Dependency of the *IF* to the calculated SSD depth and visualization of the resulting anisotropic removal topography given for (B) Sample #1 and (C) Sample #2 applying $IF > 1.5$.

obtained after PJE using equation (5). A volumetric view of topographies after anisotropic removal is shown in Figures 10B and 10C.

4.2 Scratch test sample

The evaluation method described above can not only be applied for defined static indentations shown in the previous results, but also with common scratches. In order to simulate realistic defect structures, they were generated using a scratch tester. The dynamic impact on the surface caused by a Rockwell tip can be used to model the formation of scratches caused by abrasive grains during the grinding of optical glass. The indicated mean and standard deviation of *IF* are determined for a smaller measurement matrix than provided by the original measurement. Here, two aspects must be considered. First, automatic alignment, as described in detail in Section 3.2, results in columns and rows filled with zeros. Since the scratches in the measurement field are oriented along $y = 0$, zero columns in the measurement image matrix influence the determination of the *IF*. Therefore, a reduction of the measurement matrix in x-direction is necessary. Furthermore, the extent of the scratch is low compared to the y-dimension of the measurement and would therefore bias the IF_{mean} due to an enlarged area of isotropic removal ($IF \approx 1$). Hence, the measurement matrix has to be cropped in the y-direction. In order to obtain statistically reliable *IF* values, all z^{exp} and z^{calc} matrices (see Eq. (2)) were reduced from 512 × 512 px to 476 × 160 px.

Again, the results of the *IF* calculation are compared to the slope of the VV shown in Figure 11A. Even for SSD caused by defined scratches, the highest impact of anisotropic removal (maximum of *IF* value) is present for the highest slope value (at etching removal of 12 µm). According to equation (5), a value SSD = 16.12 µm is determined. Selected surface topography measurements are shown in Figures 11B–11D. These demonstrate the significant expansion of the SSD for a surface that was previously only minorly damaged (Fig. 11B) and correlate with the plots given in Figure 11A. Figure 11B depicts scratch damage with circular structures visible at $x > 100$ µm. This plastic deformation is accompanied by crack formation and thus can also cause SSD [23] as determined with higher etching removal and verified by the corresponding *IF* values.

4.3 Conventionally ground sample

Finally, the described approach can also be applied to determine the SSD depth of mechanically ground and polished

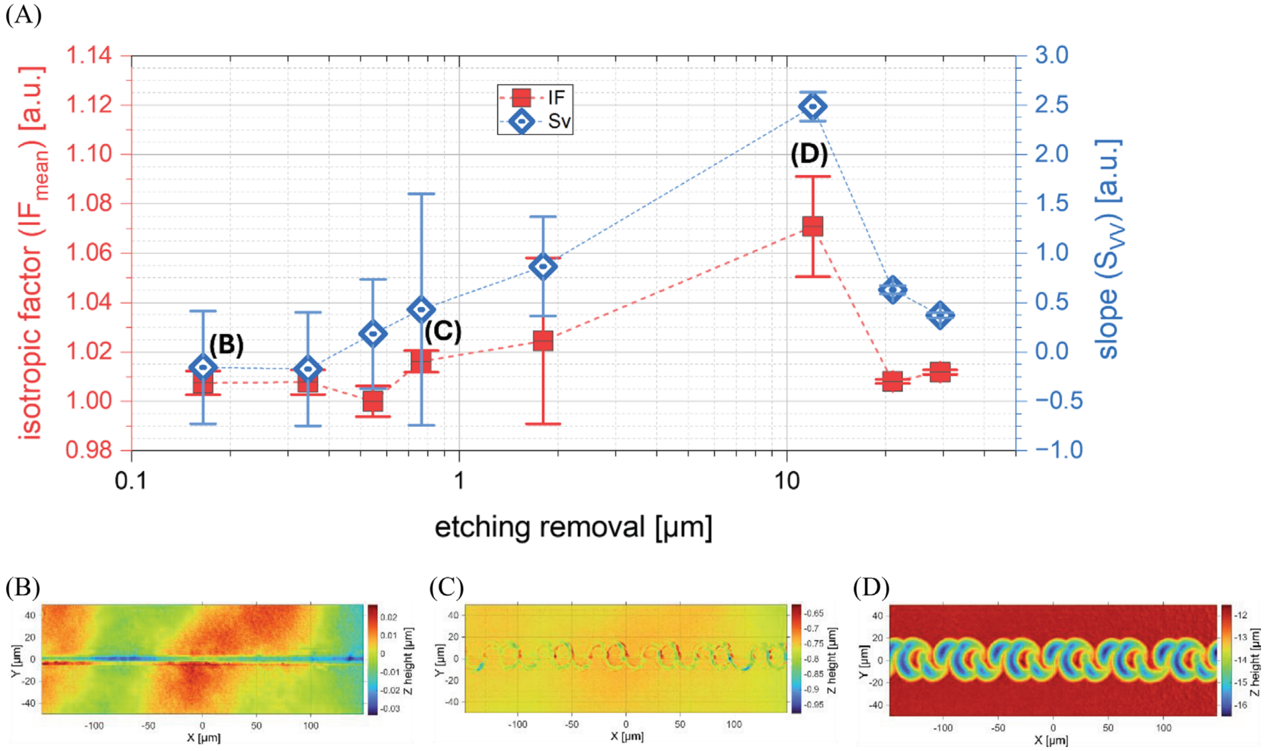

Figure 11. (A) Progress of calculated IF_{mean} and the slope, which is used to experimentally obtain the SSD depth after PJE given for Sample #3. (B–D) Surface topography maps presented for selected positions noted (A).

glass surfaces. The polishing process is intended to eliminate SSD since the extent of polishing removal exceeds the estimated damage depth from the knowledge of the manufacturing process. Despite precise lateral alignment of the samples after each PJE step in order to always measure the same area, a slight shift could not be avoided. Therefore, the measurement area had to be reduced as well in order to investigate the progress of the *IF* values for the same measurement area.

Although the initial surface shows no damage as can be seen in Figure 12A, visible defects appear after the first etching steps. These defects further develop as the etching process continues as shown in Figures 12B and 12C, reaching the maximum damage depth presented in Figure 12D. Once the maximum has been reached, uniform etching occurs in all directions as indicated by Figure 12E, causing the defect to further expand laterally. The progress of the defect in the center of the image is extracted as cross section profiles shown in Figure 12F. Since ring shaped measurement artifacts occur in the measurement, the cross sections have been fitted by a Gaussian function and shifted to zero level for better comparability. The transition from anisotropic to isotropic etch behavior after the complete removal of SSD is evident. Starting at the 8^{th} etching step (PJE #8), isotropic removal is dominant, resulting in a significant widening of defects, while further progress in depth is no longer significant.

The simultaneous surface contact with multiple abrasive grains during the grinding process results in a random distribution of defects. Nevertheless, the method for determining SSD depths can be adapted as shown in the previous examples. The calculation of *IF* results in the graph shown in Figure 13. Compared to the progress of the slope values S_{VV}, both graphs show a maximum for the same etching depth.

Since the anisotropic removal does mainly occur at a prominent defect, as shown in previous examples, the median value of *IF* was used to obtain a more reliable result. From a statistical point of view, the median offers greater robustness when dealing with outliers. In addition, the larger number of defects obtain various influences on the etching result of the respective process step. The proportion of anisotropic removal is individually dependent on depth. To some extent, the defects influence each other that small defects which are close to each other can combine to form a larger defect. The impact to the increase of *VV* is not equal over the whole measurement area. To overcome this inhomogeneity, the IF_{med} is compared to the slope value.

According to equation (5) the SSD depth of the isolated defect in measurement Sample #4 yields a value of 6.37 μm. For the overall sample, where 25 measurements after each process step have been taken into account, the SSD depth was calculated to be 8.8 μm. The example shows that the method can also be applied to determine rather shallow SSD depths. The vertical resolution of the method is approximately 1 μm and mainly depends on the etching steps chosen to identify the maximum of slope (S_{VV}) or *IF* value.

The OCT measurement provided by the University of Applied Sciences in Jena yields 9.5 μm, which shows a good agreement. Furthermore, it demonstrates that the

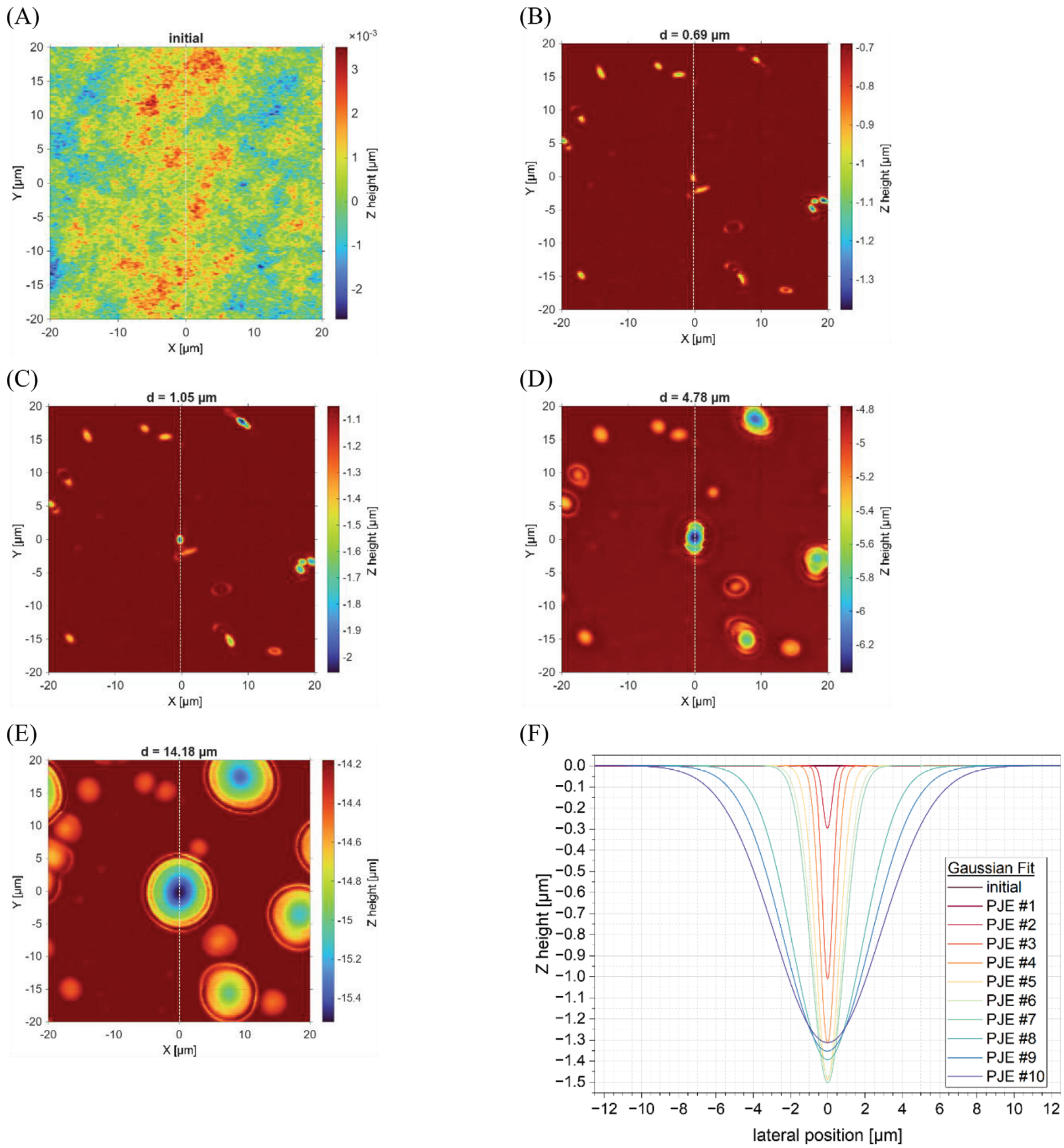

Figure 12. Surface topography measurement of a conventional manufactured fused silica surface (Sample #4): (A) initial state, (B–E) after progressive PJE, where the etching removal d is given. (F) 2D-Gaussian fit of the centered defect to visualize the progress of the SSD which is initially not present.

correlation between $IF_{\max}$ or the maximum slope S_{VV}, respectively, and SSD depth provides also a robust method for SSD characterization of conventionally manufactured samples.

5 Conclusion

The paper presents a method of destructive determination of SSD depth in fused silica surfaces by atmospheric plasma jet etching. By modeling a resulting etched surface topography assuming isotropic etching and comparison with experimentally etched surface topography, loci of anisotropic etching have been identified. Based on the analysis SSD depths were determined. Furthermore, the representation of surface positions where isotropy factors larger than 1 occur, as a depth plot help to elucidate the morphological structure of radial and median cracks causing SSD. The comparison with OCT measurements have proven the usability of the described method for SSD characterization. Hence, the developed method, eventually combined with other SSD characterization method provides valuable information for a more in-depth understanding of SSD propagation in the future.

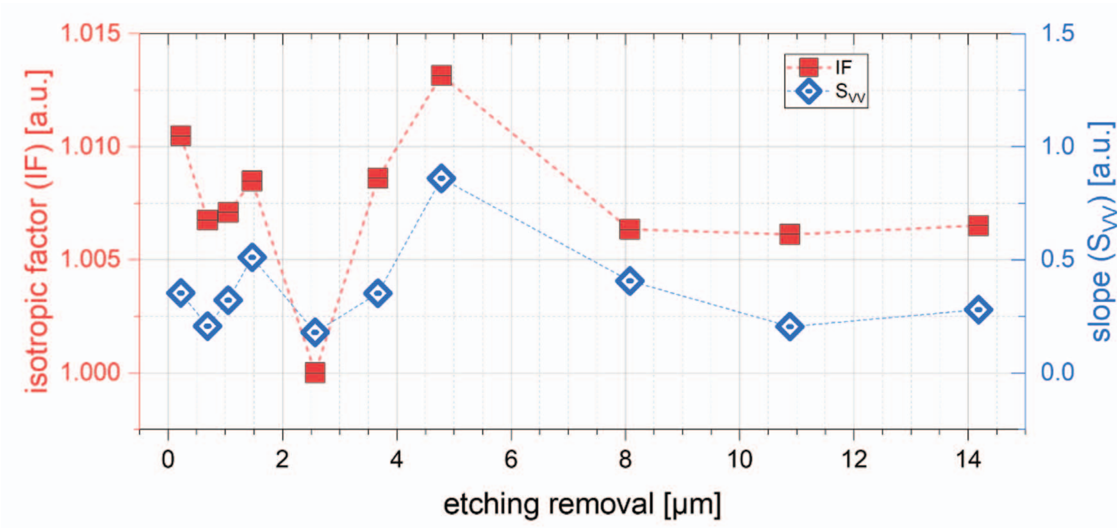

Figure 13. Comparison of calculated *IF* and the slope, which is used to experimentally obtain the SSD depth after PJE given for sample Sample #4.

Furthermore, the results can be used to validate non-destructive methods, such as OCT or laser scanning microscopy where a 3D visualization is obtained but imaging artifacts may lead to a misinterpretation of SSD depth levels.

Finally, the work presented may also be beneficial for evaluating etch results using atmospheric pressure plasma techniques employed in optics manufacturing.

Acknowledgments

The authors thank S. Frank, W. Zhang, D. Thelemann and J. Bliedtner from the University of Applied Sciences in Jena for collaboration in the project and especially providing OCT measurements for this paper. The preparation of SSD affected samples applying conventional manufacturing by Layertec GmbH is highly appreciated.

Funding

The IGF project No. 01IF22724N of the F.O.M. is funded by the Federal Ministry for Economic Affairs and Energy (BMWE) as part of the program for the promotion of industrial joint research (IGF) due to a decision of the German Bundestag.

Conflicts of interest

The authors declare that they have no competing interests.

Data availability statement

All data generated or analyzed during this study are included in this published article.

Author contribution statement

HM conducted the PJE experiments and measurements, performed analysis of the results as well as theoretical calculations, and handled the paper documentation. TA offered valuable advice for the interpretation of the data and took extensive care of correction of the manuscript to present the data more clearly. The authors have read and approved the final manuscript.

References

1. Bliedtner J, Gräfe G, in *Optiktechnologie: Grundlagen-Verfahren-Anwendungen-Beispiele*, 2nd edn. (Carl Hanser Verlag, Leipzig, 2010).
2. Yin J-F, Bai Q, Zhang B, Methods for detection of subsurface damage: a review, *Chin. J. Mech. Eng.* **31**, 1 (2018). https://doi.org/10.1186/s10033-018-0229-2.
3. Cui Y, et al., A review of subsurface damage detection methods for optical components, *AIP Adv.* **13**, 6 (2023). https://doi.org/10.1063/5.0151498.
4. Cao H, et al., Advances in subsurface defect detection techniques for fused silica optical components: A literature review, *J. Mater. Res. Technol.* **35** (2025). https://doi.org/10.1016/j.jmrt.2025.01.045.
5. Passi V et al., Anisotropic vapor HF etching of silicon dioxide for Si microstructure release, *Microelectron. Eng.* **95**, (2012). https://doi.org/10.1016/j.mee.2012.01.005.
6. Liu T et al., Hydrofluoric acid-based etching effect on surface pit, crack, and scratch and laser damage site of fused silica optics, *Opt. Exp.* **27**, 8 (2019). https://doi.org/10.1364/OE.27.010705.
7. Shu Y, Study on etching process of fused silica with concentrated HF, *Optik* **178**, (2019). https://doi.org/10.1016/j.ijleo.2018.10.011.
8. Sun L et al., KOH-based shallow etching for exposing subsurface damage and increasing laser damage resistance of fused silica optical surface, *Opt. Mater.* **108**, (2020). https://doi.org/10.1016/j.optmat.2020.110249.
9. Frank S et al., Enhanced imaging of subsurface damage in optical glass SF6 with optical coherence tomography using KOH wet etching, *EPJ Web Conf.* **309**, (2024). https://doi.org/10.1051/epjconf/202430903010.
10. Wong L et al., The effect of HF/NH4F etching on the morphology of surface fractures on fused silica, *J. Non-*

Cryst. Solids **355**, 13 (2009). https://doi.org/10.1016/j.jnoncrysol.2009.01.037.

11. Katardjiev IV, Carter G, Nobes MJ, The modelling of surface evolution during growth and erosion, *Int. J. Numer. Model.* **3**, 2 (2005). https://doi.org/10.1002/jnm.1660030209.
12. Da Costa Fernandes B et al., Understanding the effect of wet etching on damage resistance of surface scratches, *Sci. Rep.* **8**, 1 (2018). https://doi.org/10.1038/s41598-018-19716-0.
13. Krishna E, Sreelakshmy K, Medha Lal R, Comparative study on the effects of dry and wet etching on surface characteristics of fused silica optics, *Opt. Mater.* **162**, 116809 (2025). https://doi.org/10.1016/j.optmat.2025.116809.
14. Jiao P et al., Morphology evolution of Vickers indentation in fused silica glass etched by atmospheric pressure plasma jet, *Ceram. Int.* **48**, 21 (2022). https://doi.org/10.1016/j.ceramint.2022.07.069.
15. Meister J, Arnold T, New process simulation procedure for high-rate plasma jet machining, *Plasma Chem. Plasma Process.* **31**, 1 (2010). https://doi.org/10.1007/s11090-010-9267-y.
16. Arnold T, Böhm G, Paetzelt H, Ultra-precision surface machining with reactive plasma jets, *Contrib. Plasma Phys.* **54**, 2 (2014). https://doi.org/10.1002/ctpp.201310058.
17. Müller, H et al., Atmospheric plasma jet processing for figure error correction of an optical element made from S-BSL7, *J. Eur. Opt. Soc. Rapid Publ.* **18**, 1 (2022). https://doi.org/10.1051/jeos/2022003.
18. Ehrhardt M et al., Transfer of micron pattern with reactive atmospheric plasma jets into fused silica, *Appl. Surf. Sci. Adv.* **23**, (2024). https://doi.org/10.1016/j.apsadv.2024.100636.
19. Arnold T, Boehm G, Paetzelt H, New freeform manufacturing chains based on atmospheric plasma jet machining, *J. Eur. Opt. Soc.: Rapid Publ.* **11**, 16002 (2016). https://doi.org/10.2971/jeos.2016.16002.
20. Vickers hardness test procedure (Web pages, cited 2026 30-01). https://www.tec-science.com/material-science/material-testing/vickers-hardness-test/.
21. Diamond cone for Rockwell hardness testing (Web pages, cited 2026 30-01). https://www.tec-science.com/material-science/material-testing/rockwell-hardness-test/.
22. Müller H, Arnold T. in *Proceedings of the Twelfth European Seminar on Precision Optics Manufacturing, Teisnach (Germany)*, 2025, edited by G. Fütterer, C. Wünsche, O.W. Fähnle, H. Thieß, A. Haberl (Proc. SPIE), 1378906, https://doi.org/10.1117/12.3074295.
23. Zakiev, I et al., Glass fracture during micro-scratching, *Surfaces* **3**, 2 (2020). https://doi.org/10.3390/surfaces3020016.